

Pillar in Pillar: Multi-Scale and Dynamic Feature Extraction for 3D Object Detection in Point Clouds

Yonglin Tian^{1,2}, Lichao Huang³, Xuesong Li², Yuan Li³, Zilei Wang¹, Fei-Yue Wang²

¹University of Science and Technology of China

²The State Key Laboratory for Management and Control of Complex Systems,
Institute of Automation, Chinese Academy of Sciences

³Horizon Robotics

Abstract

Sparsity and varied density are two of the main obstacles for 3D detection networks with point clouds. In this paper, we present a multi-scale voxelization method and a decomposable dynamic convolution to solve them. We consider the misalignment problem between voxel representation with different scales and present a center-aligned voxelization strategy. Instead of separating points into individual groups, we use an overlapped partition mechanism to avoid the perception deficiency of edge points in each voxel. Based on this multi-scale voxelization, we are able to build an effective fusion network by one-iteration top-down forward. To handle the variation of density in point cloud data, we propose a decomposable dynamic convolutional layer that considers the shared and dynamic components when applying convolutional filters at different positions of feature maps. By modeling bases in the kernel space, the number of parameters for generating dynamic filters is greatly reduced. With a self-learning network, we can apply dynamic convolutions to input features and deal with the variation in the feature space. We conduct experiments with our PiPNet on KITTI dataset and achieve better results than other voxelization-based methods on 3D detection task.

1. Introduction

3D object detection plays a great role in autonomous driving and intelligent transportation. LiDAR sensor is one of the key factors to achieve precise localization for 3D detection systems. However, the sparsity and uneven distribution of LiDAR data heavily restrict the effective extraction of features from point cloud. Lots of works have been proposed to handle these problems. PointNet [17, 18] designs a network to directly process unordered point cloud. It transforms the feature of each point to a high-dimension space

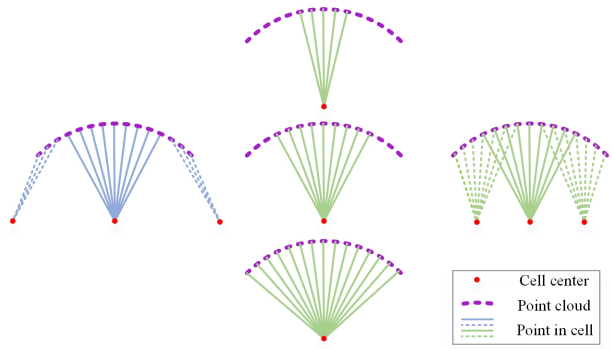


Figure 1. Illustration of our multi-scale voxelization method. Left: Dividing point cloud with single and individual voxels. Middle: Our center-aligned multi-scale voxelization method. Right: Our method also enables the interaction between different voxels to avoid perception deficiency of edge points.

and aggregates point features using max pooling. With the proper partition [18] of the whole data, PointNet can well settle the trouble in local and global features extraction for point cloud, thus becoming a basic component in many 3D detection networks [27, 16, 25, 23, 10]. Voxelization-based approaches [27, 25, 10] combine PointNet with existing CNNs. They divide point cloud into voxels or pillars and reformat the data into a regular shape. Then, PointNet is applied to generate local features for each small point set and CNNs are used to further process these structural features.

This kind of voxelization eases the difficulty of detection from unordered point cloud, however, it affects the perception of points on the edge of each group during voxel feature encoding and neglects the uneven distribution of point cloud. On the one hand, all these methods [27, 25, 10] map a point into a single voxel or pillar and yield the feature by aggregating the features of points within the same group as shown in Figure 1 (left part). This is against the per-

ception of local features. Points near the voxel edge can only perceive information from part of its neighbors during voxel feature encoding and thus leading to the perception deficiency. On the other hand, considering that the density of points varies with the distance to LiDAR center, grouping points with voxel or pillar with one size is insufficient. For example, position far from the sensor deserves a larger volume to fully extract the local features. VoxelFPN [22] considers the use of multi-scale voxelization and achieves better performance. However, it ignores the perception deficiency of edge points and the misalignment problem between point representation with different scales as shown in Figure 2. This kind of misalignment may enlarge the bias between multi-scale features and affect the performance of detection model. In our method, instead of partitioning point cloud with isolated and single-scale voxels, we propose a new way to gather richer features from unordered points as illustrated in Figure 1 (middle and right parts). We adopt a center-aligned multi-scale strategy to generate robust local features. An overlapped voxelization mechanism is used to avoid the perception deficiency problem of edge points. In this way, edge points of one voxel can be reconsidered in another voxel where more neighbors can be accessed to produce more sufficient features.

With voxelized dense features, many works [10, 25, 27] have utilized CNNs to make final predictions. Although CNNs have achieved great successes in many tasks like computer vision and pattern recognition, making precise prediction for objects with heavily changing appearances is still hard for them [7]. Taking LiDAR data as an example, the number of points generated from the same object can decrease from a few hundred to several as the object moves away. It is tough for CNNs to regress same objectives from diverse features. Dynamic filter network (DFN) [8] proposes to cope with such changes with adaptive filters learned by an extra network and has been successfully applied in tasks, such as depth completion [21] and image classification [3]. However, replacing traditional convolution filters with corresponding dynamic ones will greatly increase the number of parameters. To reduce the computation and get better modeling of the kernel space, we propose a new convolutional layer named decomposable dynamic convolution (DD-Conv) that decomposes the convolution into shared and dynamic parts. Shared part is used to extract common features among different inputs and dynamic part focuses on the changing of the data. Instead of directly regressing the parameters of dynamic filters, we further decompose it into the building of bases for the kernel space and the learning of coefficients. Therefore, a dynamic filter can be generated by the combination of several approximated bases.

Our main contributions can be summarized as follows:

- We propose a multi-scale voxelization method to gen-

erate robust features, which avoids the perception deficiency of edge points from each voxel and well solves the misalignment problem.

- An effective fusion network is designed to combine multi-scale features through a single top-down forward.
- We put forward a novel decomposable dynamic convolutional layer that can well handle the variety of input features and greatly reduce the parameters of dynamic filters.
- We achieve better results than other voxelization-based methods on KITTI benchmark for *car* and *cyclist* classes.

2. Related Work

2.1. 3D detection from raw point clouds

PointNet [17] is the pioneer to directly manipulate raw point clouds with neural networks. It is efficient and effective to process unordered data and lays the foundation for many 3D detection networks [16, 19, 26, 15]. The main difference among these methods is the generation of proposals. F-PointNet [16] generates frustum-shaped proposals in point cloud with the help of 2D detection and uses PointNet to segment positive points for the regression of 3D bounding box. VoteNet [15] gets rid of the rely on 2D detection to propose 3D boxes and demonstrates a new proposal generation mechanism with deep Hough voting [6]. It claims that voting from seed points helps with the generation of more confident and accurate proposals. Point RCNN [19] turns to point segmentation network for the generation of 3D proposals. Different from F-PointNet, Point RCNN directly segments the whole point cloud and produces proposal for each foreground point.

2.2. Voxelization-based 3D detection from point clouds

Voxelization-based approaches for point cloud processing turn irregular points into an ordered tensor to simplify the extraction of features and make full use of mature CNNs. MV3D [2] and AVOD [9] propose to slice the point cloud into several layers and divide each layer into small grids. The maximum height in each grid is extracted to generate height maps. Together with other features and image data, they design multi-view networks for 3D detection. Instead of using handcrafted features to represent each small region, VoxelNet [27] proposes a data-driven method using PointNet to get richer representation for each voxel. To accelerate the convolution of sparse data after voxelization, SECOND [25] applies a sparse convolution algorithm and achieves real-time inference. To avoid 3D convolution operation and further speed up 3D detection, PointPillars [10]

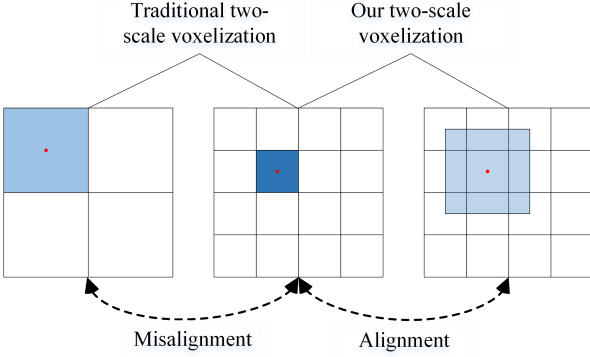


Figure 2. Illustration of the misalignment problem introduced by traditional voxelization and our center-aligned voxelization method.

enlarges voxel to pillars which ignores the partition along z axis and achieves satisfactory accuracy and speed. However, all these methods take voxels as individual groups at the early stage. The edge points of each voxel suffer from the perception deficiency problem because only part of their neighbors can be accessed during voxel feature encoding. And most methods only consider the single-scale voxelization and ignore the uneven distribution of LiDAR point.

2.3. Dynamic filter networks

DFN [8] introduces a new framework that can generate dynamic filters depending on the input. It uses an extra network to output the parameters of filters for every position of the input and enables adaptive feature extraction. ECC [20] extends dynamic filters to graph and demonstrates the effectiveness on point cloud classification. To incorporate more information in the neighbour regions, LS-DFN [24] generates weights with larger receptive fields using dynamic sampling convolution. Tang et al. [21] propose to take image features as the guidance to generate the weights used for depth completion. To reduce the GPU memory consumption, they factorize the dynamic convolution into channel-wise and cross-channel convolution. We share the same philosophy with these methods to dynamically generate position-specific filters, but we treat the problem in a different way. In our approach, the kernel space is decomposed into shared part and dynamic part. To make the filters easier to learn and reduce memory usage, we treat the dynamic part as the combination of several principle components.

3. PiPNet

The framework of our PiPNet is illustrated in Figure 3. The main components of our detection network include the multi-scale pillar feature generation, a top-down fusion net-

work and a dynamic detection head.

3.1. Multi-scale voxelization

We first crop the whole point cloud into a cube where the coordinates of each point are ranging in $[[x_{min}, x_{max}], [y_{min}, y_{max}], [z_{min}, z_{max}]]$. Then, we divide the region into grid along x and y axes with size of x_s, y_s respectively and ignore the division along vertical direction like [10]. Each cell has the size of S .

$$S = [x_s, y_s, z_{max} - z_{min}]. \quad (1)$$

And the set of all cells can be denoted as:

$$C = \{c_j | j = 1, \dots, H * W\}, \quad (2)$$

where c_j is the j -th cell in the grid. H and W are the height and width of the grid:

$$H = \left\lceil \frac{x_{max} - x_{min}}{x_s} \right\rceil; \quad (3)$$

$$W = \left\lceil \frac{y_{max} - y_{min}}{y_s} \right\rceil.$$

In our multi-scale voxelization algorithm, we introduce a center-aligned mechanism. We define K pillars for each cell to collect points within their range and the range size of k -th pillar is:

$$[k \cdot x_s, k \cdot y_s, z_{max} - z_{min}]. \quad (4)$$

We define one corresponding filter for each size of pillar and the pillar filters set F can be denoted as follows:

$$F = \{f_k | k = 1, \dots, K\}. \quad (5)$$

For every non-empty cell, we apply pillar filters to gather the point information in each pillar. It is worth noting that all these pillar filters are centered on the non-empty cell to avoid the misalignment problem. To reduce the information redundancy caused by the overlapping of such filters, we define different strategies for filters with different sizes. For the smallest filter f_1 , we define the filter as follows:

$$f_1(p_{j1}) = \{[x_i, y_i, z_i, x_{ci}, y_{ci}, z_{ci}, x_{pi}, y_{pi}, r], i = 1, \dots, N_{j1}\}. \quad (6)$$

For $k > 1$, we have:

$$f_k(p_{jk}) = \{[x_{ci}, y_{ci}, z_{ci}, x_{pi}, y_{pi}, r], i = 1, \dots, N_{jk}\}. \quad (7)$$

where p_{jk} is the pillar corresponding to filter f_k in the position of cell j . N_{jk} is the number of points in pillar k for cell j . $[x_i, y_i, z_i]$ is the coordinates of point in pillar p_{jk} in LiDAR coordinate system. $[x_{ci}, y_{ci}, z_{ci}]$ is coordinates relative to the mean of all points within the pillar. $[x_{pi}, y_{pi}]$ is

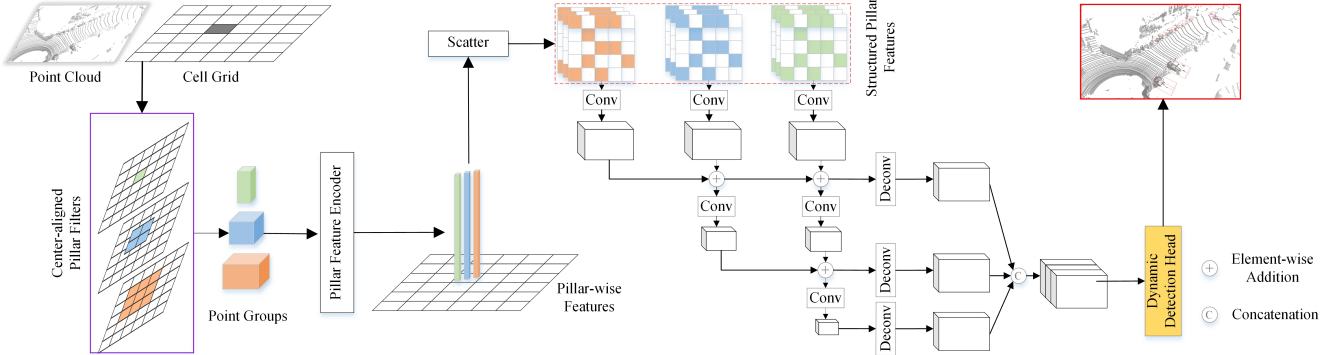


Figure 3. The framework of PiPNet. First, the whole point cloud is divided into grids along x and y axes. For non-empty cells in the grid, we apply several center-aligned filters with different scales and gather the points within the range of each filter. Then, Pillar feature encoder is used to generate pillar-wise features. After the scatter operation like [10], we get structural features for different pillar filters. A top-down fusion network is designed to fuse multi-scale features. Our dynamic detection head outputs the final detection results with fused features.

coordinates relative to the center of pillar p_{jk} and z coordinate is ignored. The reflectance is denoted as r .

After the grouping and preprocessing of pillar filters, we get several point groups for each cell. To reduce memory usage and get more representative features of each cell, we only consider the pillars corresponding to non-empty cells and store their positions. For every scale, a simple PointNet is used to extract the features of points in each pillar which first extends the dimension of each point to 64 and generate the local feature vector of the pillar with a max pooling operation. We use stored positions of non-empty cells to scatter these feature vectors into structural feature maps.

3.2. Top-down fusion network

Benefiting from our multi-scale voxelization method, we get multiple feature maps with different receptive fields. Therefore, we are able to build effective fusion network through one top-down pathway instead of using both top-down and bottom-up pathways like FPN [12]. We iteratively add features with large scale to smaller ones and terminate the processing of large-scale features to reduce computation and memory usage. We totally use three kinds of convolutional blocks in our fusion network. The stride, number of convolutional layers and number of output channels of each block are $[s, 3, 64]$, $[2s, 5, 128]$, $[4s, 5, 256]$ and we set s to 2 for the detection of *car* and 1 for *cyclist*. The output of each block is up-sampled to the same size and concatenated for the detection head.

3.3. Decomposable dynamic convolution

Traditional convolutional layer takes structural feature maps as inputs which can be denoted as $I \in \mathbb{R}^{h \times w \times c}$ and output new feature maps $O \in \mathbb{R}^{h' \times w' \times c'}$ using multiple filters with weights $W \in \mathbb{R}^{s \times s \times c \times c'}$. Here, h , w and c are the

height, width and number of channels of input feature. And h' , w' and c' are size of output feature. The kernel size is denoted by s . Traditional convolution can be formalized as:

$$O = W \otimes I. \quad (8)$$

And our decomposable dynamic convolution is compatible with traditional convolution. It is comprised of two parts, i.e., dynamic weights generation and shared weights generation as shown in Fig. 4. We formulate our DD-Conv as follows:

$$O = (W_d(I; \theta_d) + W_s(I; \theta_s)) \hat{\otimes} I, \quad (9)$$

where θ_d and θ_s are the parameters of networks to learn the dynamic weights $W_d \in \mathbb{R}^{h \times w \times s \times s \times c \times c'}$ and shared weights $W_s \in \mathbb{R}^{s \times s \times c \times c'}$ (To combine the dynamic and shared weights together, we simply replicate W_s to $W_s \in \mathbb{R}^{h \times w \times s \times s \times c \times c'}$). $\hat{\otimes}$ is the position-dependent convolution operation. The weights of our convolution is varied with the position of sliding window which is the main difference compared with traditional convolution.

3.3.1 Dynamic weights generation

We factorize the generation of dynamic weights into the construction of kernel space and the learning of coefficient vectors. We use a set of tensors as approximated bases and learn a coefficient vector at each position for each tensor to make the target convolution kernel both input-dependent and position-dependent.

We assume that the kernel space can be approximated by a set of M representative tensors denoted as $V = \{v_i | v_i \in \mathbb{R}^{s \times s \times c \times c'}, i = 1, \dots, M\}$. We can apply an extra network G_{dk} to generate these tensors or just treat these tensors as

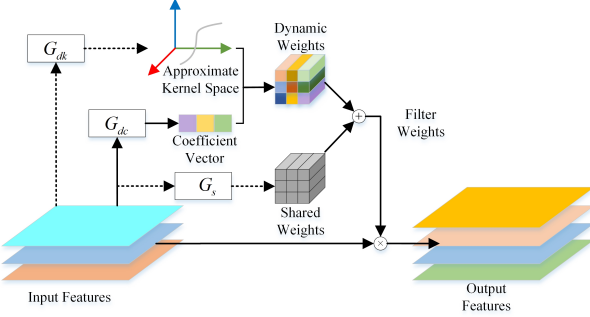


Figure 4. Illustration of our decomposable dynamic convolution.

model parameters [8] as these in traditional convolutional layers.

Based on these representative tensors, we build a network G_{dc} to regress the coefficient of each tensor for different inputs and positions. We denote the output of G_{dc} as $C_d \in \mathbb{R}^{h \times w \times M}$, which is both input-dependent and position-dependent. Then, the dynamic weights of filters at the position $[i, j]$ of specific feature maps can be expressed as:

$$W_d[i, j] = C_d[i, j] \times [v_1, \dots, v_M] \quad (10)$$

3.3.2 Shared weights generation

Shared weights $W'_s \in \mathbb{R}^{s \times s \times c \times c'}$ are introduced mainly for the capture of common representations among all positions of the input feature. They can either be generated with network G_s or defined as model parameters.

Our combination of shared and dynamic weights decouples the perception of varied patterns. Although dynamic parts are theoretically capable of depicting the feature space, it will ease the task with both shared and dynamic parts considered. Taking the detection of cars from point cloud as an example, point density of different samples varies with the condition of the sample. However, they share some common features more or less because they are from the same kind of object. Therefore, the deployment of both position-independent shared filters and position-dependent dynamic filters is potential to achieve robust perception of changeable objects.

The total number of parameters of generated filters in our DD-Conv is $s \times s \times c \times c' \times (M + 1) + h \times w \times M$ where dynamic part contains $s \times s \times c \times c' \times M + h \times w \times M$ parameters and shared part contains $s \times s \times c \times c'$ ones. Compared with DFN [8], our DD-Conv greatly reduces the memory usage especially for feature maps with large size. The ratio of memory usage between our DD-Conv and DFN

is:

$$\begin{aligned} \frac{Mem_{our}}{Mem_{dfn}} &= \frac{s \times s \times c \times c' \times (M + 1) + h \times w \times M}{s \times s \times c \times c' \times h \times w} \\ &= \frac{M + 1}{h \times w} + \frac{M}{s \times s \times c \times c'} \end{aligned} \quad (11)$$

As an example, with $s = 3, c = 128, c' = 128, h = 248, w = 216, M = 3$, The memory consumed by the filters of DFN is 10,524 times than us.

4. Loss

We adopt similar loss design as [10] which is composed of three parts. The ground truth boxes and anchors are defined as $[x^{gt}, y^{gt}, z^{gt}, w^{gt}, l^{gt}, h^{gt}, \theta^{gt}]$ and $[x^a, y^a, z^a, w^a, l^a, h^a, \theta^a]$ respectively. The residual targets between ground truth and anchors are defined by:

$$\begin{aligned} \Delta x &= \frac{x^{gt} - x^a}{d^a}, \Delta y = \frac{y^{gt} - y^a}{d^a}, \Delta z = \frac{z^{gt} - z^a}{h^a}, \\ \Delta w &= \log \frac{w^{gt}}{w^a}, \Delta l = \log \frac{l^{gt}}{l^a}, \Delta h = \log \frac{h^{gt}}{h^a}, \\ \Delta \theta &= \sin(\theta^{gt} - \theta^a), \end{aligned} \quad (12)$$

where $d^a = \sqrt{(w^a)^2 + (l^a)^2}$. The localization loss is:

$$\mathcal{L}_{loc} = \sum_{b \in (x, y, z, w, l, h, \theta)} SmoothL1(\Delta b). \quad (13)$$

Localization loss is defined as focal loss [13] as follows:

$$\mathcal{L}_{cls} = -\alpha(1 - p^a)^\gamma \log p^a, \quad (14)$$

where $\alpha = 0.25, \gamma = 2$, p^a is the classification probability. To distinguish the flipped boxes, a softmax loss \mathcal{L}_{dir} is added to learn the direction. Therefore, the total loss for detection task is:

$$\mathcal{L} = \frac{1}{N_{pos}}(\beta_{loc}\mathcal{L}_{loc} + \beta_{cls}\mathcal{L}_{cls} + \beta_{dir}\mathcal{L}_{dir}), \quad (15)$$

where N_{pos} is the number of positive anchors and $\beta_{loc} = 2.0, \beta_{cls} = 1.0$ and $\beta_{dir} = 0.2$.

To diverge the representative tensors of our DD-Conv and make them orthogonal with each other as much as possible, we add a similarity loss using normalized dot products between different tensors as follows. When we use DD-Conv in our network, the similarity loss is added with detection loss with a coefficient of 0.1.

$$\mathcal{L}_{sim} = \frac{1}{M} \sum_{i, j \in [1, \dots, M]; i < j} \frac{|v_i \cdot v_j|}{\|v_i\|_2 \cdot \|v_j\|_2}. \quad (16)$$

Method	Modality	AP (IoU=0.7)		
		Moderate	Easy	Hard
MV3D [2]	RGB & LiDAR	62.68	71.29	56.56
ContFuse [11]	RGB & LiDAR	73.25	86.32	67.81
AVOD-FPN [9]	RGB & LiDAR	74.44	84.41	68.65
F-PointNet [16]	RGB & LiDAR	70.92	83.76	63.65
VoxelNet [27]	LiDAR	65.46	81.98	62.85
SECOND [25]	LiDAR	76.48	87.43	69.10
Ours	LiDAR	78.23	88.34	76.31

Table 1. Performance of 3D object detectors on the *car* class of the KITTI *val* set.

Method	Modality	AP (IoU=0.7)		
		Moderate	Easy	Hard
MV3D [2]	RGB & LiDAR	78.10	86.55	76.67
F-PointNet [16]	RGB & LiDAR	84.02	88.16	76.44
ContFusion [11]	RGB & LiDAR	87.34	95.44	82.43
VoxelNet [27]	LiDAR	84.81	89.60	78.57
SECOND [25]	LiDAR	87.07	89.96	79.66
Ours	LiDAR	88.05	90.38	86.33

Table 2. Performance of BEV object detection on the *car* class of the KITTI *val* set.

5. Experiments

We conduct our experiments on KITTI dataset [4]. Details of our network and experiments are demonstrated in Sec. 5.1. The comparison with other methods are shown in Sec. 5.2. In Sec. 5.3, ablation studies are conducted to analyze our proposed method.

5.1. implementation details

During the voxelization stage, we first crop the whole point cloud within the range $[-39.68, 39.68]$, $[0, 69.12]$, $[-1, 3]$. The size of cell is set as $[0.16, 0.16, 4]$ and we use three kind of pillars which have size of $[0.16, 0.16, 4]$, $[0.32, 0.32, 4]$ and $[0.48, 0.48, 4]$ respectively.

For the decomposable dynamic convolution, we use three representative tensors in all experiments unless explicitly varied in ablation study. We use a two-layer generation network in all the DD-Conv which contains a bottleneck layer and an output layer.

Following the split manner in [2], the training set of KITTI dataset is divided into *train* set (3712 images) and *val* set (3769 images). We use an Adam optimizer to train our network. The learning rate is set as 0.0002 initially and decays by a factor of 0.8 for every 15 epochs. We train our network for 160 epochs with a batch size of 2 using a NVIDIA Titan V GPU card.

5.2. Results

We evaluate our network on KITTI dataset for both validation set and the official test benchmark for *car* and *cyclist*. Table 1 and Table 2 show our results on validation set for 3D and bird eye’s view (BEV) detection individu-

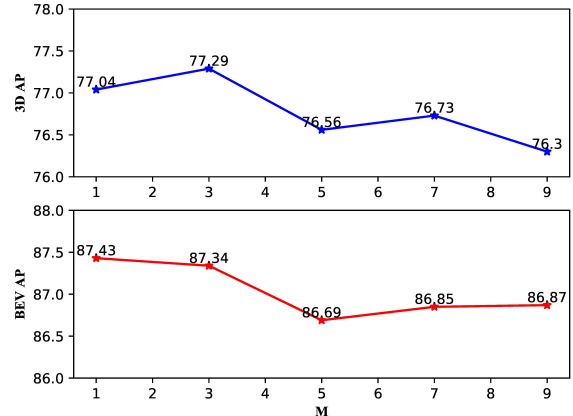


Figure 5. 3D and BEV AP change over the number of representative tensors (M) on *car* class of KITTI *val* set.

ally. In Table 3 and Table 4, we show our results on the KITTI benchmark. Due to the evaluation policy change of KITTI benchmark on 08.10.2019 that replaces the 11 recall positions with 40 ones, we can only get the results from the benchmark with 40 recall positions after the policy change. To make a fair comparison with previous works, we maintain both results of these works before and after the change.

We achieve the top performance among all the voxelization-based methods on 3D detection test benchmark for *car* and *cyclist* classes under *moderate* mode. We outperform PointPillars [10] for all the entries on the test set for *car* class. We are 1.93, 2.72 and 1.46 points higher than PointPillars on the 3D detection task for *car* under three modes. It demonstrates the effectiveness of our multi-scale strategy and dynamic convolutional layer.

5.3. Ablation study

In this part, we analyze each component in our network. We make all the experiments on the *car* class of KITTI validation set. For our baseline network, we use a single scale of pillar and use traditional convolutional layers. Table 5 shows the gains of performance by introducing multi-scale strategy and our dynamic convolution. When we use dynamic filters without multi-scale pillars, we change every convolutional layer to our DD-Conv. But, we only replace the convolution layer in detection head to our dynamic convolution when we use both the multi-scale strategy and dynamic filters to reduce the computation. Our multi-scale fusion and dynamic filtering alleviate the density variation of point cloud and remarkably increase the AP for 3D detection. We are 1.99, 2.8 and 5.73 point higher than the baseline under *moderate*, *easy* and *hard* mode.

Figure 5 illustrates the variation of AP on 3D and BEV detection for *car* class when we use different number of representative tensors (denoted as M). When $M = 3$, we

Method	Modality	Speed/Hz	Car (3D)			Car (BEV)		
			Moderate	Easy	Hard	Moderate	Easy	Hard
MV3D [2]	RGB + LiDAR	2.8	63.63 / 62.35	74.97 / 71.09	54.00 / 55.12	78.93 / 76.90	86.62 / 86.02	69.80 / 68.49
ContFuse [11]	RGB + LiDAR	16.7	- / 66.22	- / 82.54	- / 64.04	- / 85.83	- / 88.81	- / 77.33
AVOD-FPN [9]	RGB + LiDAR	10	71.76 / 71.88	83.07 / 81.94	65.73 / 66.38	84.82 / 83.79	90.99 / 88.53	79.62 / 77.90
F-PointNet [16]	RGB + LiDAR	5.9	69.79 / 70.39	82.19 / 81.20	60.59 / 62.19	84.67 / 84.00	91.17 / 88.70	74.77 / 75.33
VoxelNet [27]	LiDAR	4.4	- / 65.11	- / 77.47	- / 57.73	- / 79.26	- / 89.35	- / 77.39
SECOND [25]	LiDAR	20	72.55 / 73.66	83.34 / 83.13	65.82 / 66.20	83.77 / 79.37	89.39 / 88.07	78.59 / 77.95
PointPillars [10]	LiDAR	62	74.31 / 74.99	82.58 / 79.05	68.99 / 68.30	86.56 / 86.10	90.07 / 88.35	82.81 / 79.83
Ours	LiDAR	20	76.24 / -	85.30 / -	70.45 / -	87.25 / -	90.87 / -	83.38 / -

Table 3. Performance evaluation on KITTI 3D and BEV detection test server for *car*.

Method	Modality	Cyclist (3D)			Cyclist (BEV)		
		Moderate	Easy	Hard	Moderate	Easy	Hard
AVOD-FPN [9]	RGB + LiDAR	50.55 / 52.18	63.76 / 64.00	44.93 / 46.61	57.12 / 57.48	69.39 / 68.09	51.09 / 50.77
F-PointNet [16]	RGB + LiDAR	56.12 / 56.77	72.27 / 71.96	49.01 / 50.39	61.37 / 61.96	77.26 / 75.38	53.78 / 54.68
VoxelNet [27]	LiDAR	- / 48.36	- / 61.22	- / 44.37	- / 54.76	- / 66.70	- / 50.55
SECOND [25]	LiDAR	52.08 / 53.85	71.33 / 70.51	45.83 / 40.90	56.05 / 56.04	76.50 / 73.67	49.45 / 48.78
PointPillars [10]	LiDAR	58.65 / 59.07	77.10 / 75.78	51.92 / 52.92	62.73 / 62.25	79.90 / 79.14	55.58 / 56.00
Ours	LiDAR	59.54 / -	75.43 / -	53.37 / -	65.12 / -	79.51 / -	58.25 / -

Table 4. Performance evaluation on KITTI 3D and BEV detection test server for *cyclist*.

Configuration	multi-scale	3D AP (IoU=0.7)		
		Moderate	Easy	Hard
\times	\times	75.86	85.21	69.51
\times	\checkmark	77.29	86.88	72.88
\checkmark	\times	77.85	88.01	75.24
\checkmark	\checkmark	78.25	88.34	76.31

Table 5. Performance of 3D object detectors with different configurations on the *car* class of the KITTI *val* set.

Configure	3D AP		
	Moderate	Easy	Hard
DD-Conv (without shared part)	76.84	86.86	70.24
DD-Conv (with shared part)	77.29	86.88	72.88

Table 6. Performance of DD-Conv with and without shared part on the *car* class of the KITTI *val* set.

achieve a better results. The AP decreases more or less when we use more representative tensors in our dynamic convolution. This may be caused by our simple coefficient learning network G_{dc} . With only a bottleneck and an output layer, learning the relationship between too many tensors can be a hard task. In Table 6, we illustrate the influence of shared weights in our DD-Conv. With shared weights, we achieve better results especially for *hard* objects.

To illustrate the effectiveness of our multi-scale strategy, we remove the DD-Conv layers in our network and compare our results with VoxelFPN [22]. VoxelFPN doesn't consider the misalignment problem and adopts a top-down bottom-up fusion style. Table 7 shows the results of VoxelFPN and our method. Even we don't use SSD head [14] and FPN [12] fusion style, we still outperform VoxelFPN using three scales and achieve comparable results under two scales.

Table 8 shows the comparison of different dynamic filters. Due to the huge memory usage of DFN [8], it can only be used in the detection head of our network. To make

a fair comparison, we only replace the layer in detection head with different dynamic filters and keep other layers unchanged. In our detection head, we take the input with size [248, 216, 386] and output the detection results with shape [248, 216, 20] (each position has 2 anchors and each anchor needs 7 box targets, 1 classification target and 2 direction targets). For Depth-aware convolution [1], we set the number of bins to 27 like [1] which is claimed to have the best performance compared with other choices. Compared with DFN [8], we reduce the number of parameters generated by the dynamic convolution layer from 413,544,960 to 23,160 while achieve comparable results. This greatly reduce the cost of integrating dynamic layers into existing models. Different from the predefined rows in Depth-aware convolution layer [1], our filters are much more flexible which can generate position-specific filters varying with input features at different positions.

Our decomposable dynamic convolution can be conveniently plugged into existing convolutional neural models without any extra change. We conduct experiments on two of the typical voxelization-based models, PointPillars [10] and SECOND [25]. In our implementation, we reproduce these two network and replace traditional convolutional layers with our DD-Conv. The results are shown in Table 9. We witness a much higher promotion in PointPillars than SECOND. It is probably related to the usage of sparse convolution [5] in SECOND which claims to better cope with sparse point cloud. We visualize the coefficient vector of our DD-Conv for classification head in Figure 6. We can see that our dynamic filters are capable of responding differently to positive and negative samples. This kind of difference may help the network to decompose a task into smaller chunks and solve factorized problems intently using different filters. Besides, different reactions are also observed

Method	Configuration			3D AP		
	scales	FPN	SSD	<u>Moderate</u>	Easy	Hard
VoxelFPN	3	X	✓	76.36	86.07	69.34
Our	3	X	X	77.85	88.01	75.24
VoxelFPN	2	✓	✓	77.70	88.42	76.03
Our	2	X	X	77.73	87.85	76.13

Table 7. Comparison with detectors using different multi-scale strategies on the *car* class of the KITTI *val* set.

Method	3D AP			Parameters
	<u>Moderate</u>	Easy	Hard	
Baseline	75.86	85.21	69.21	-
DFN[8]	77.02	87.23	70.10	413,544,960
Depth-aware [1]	76.40	84.61	69.63	208,440
Ours	77.06	86.40	70.16	23,160

Table 8. Performance of 3D object detectors with different dynamic filters on the *car* class of the KITTI *val* set.

Method	3D AP		
	<u>Moderate</u>	Easy	Hard
PointPillars	75.86	85.21	69.21
PointPillars(with DD-Conv)	77.29	86.88	72.88
SECOND	77.98	87.98	76.83
SECOND(with DD-Conv)	78.48	88.62	77.11

Table 9. Performance of 3D object detectors before and after using DD-Conv on the *car* class of the KITTI *val* set.

among positive samples. We take distance as a key property of object because it's highly related to the density and quality of points. We sample 300 LiDAR data from our validation set. The distance of every *car* and the corresponding coefficient vector are shown Figure 7. We can see that coefficient vector varies with the distance of the object in a statistical sense. It verifies our intuition to handle highly changeable objects with different filter in a dynamic manner. Figure 8 shows the similarity of representative tensors of our DD-Conv. With the similarity loss, the generated tensors are approximately orthogonal.

6. Conclusion

In this paper, we propose a new multi-scale fusion strategy and a decomposable dynamic convolutional layer in our voxelization-based PiPNet. We adopt a center-aligned voxelization method which alleviates the misalignment problem between feature maps with different scales. To avoid the perception deficiency of edge points, we use overlapped partition rather than isolated ones. Our dynamic convolutional layers decompose convolution into shared and dynamic parts. We innovatively take dynamic filtering as the learning of representative tensors and combination of them. This insight helps us greatly reduce the number of parameters and ease the difficulty to fit varying features in point cloud. We take our experiments on KITTI dataset and achieve top performance compared with other voxelization-based methods.

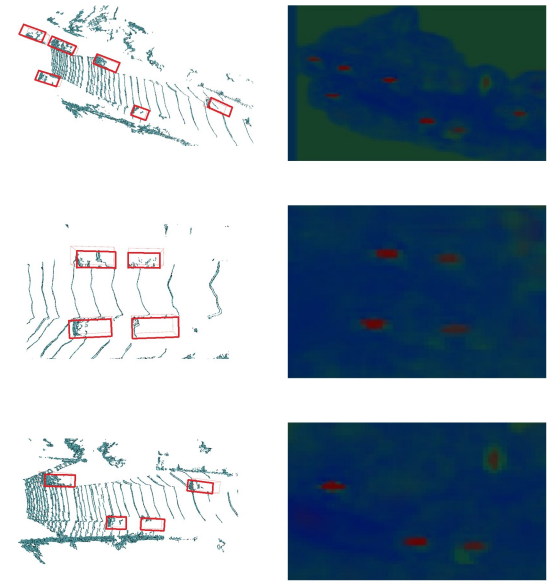


Figure 6. Visualization of the coefficient vectors in our DD-Conv.

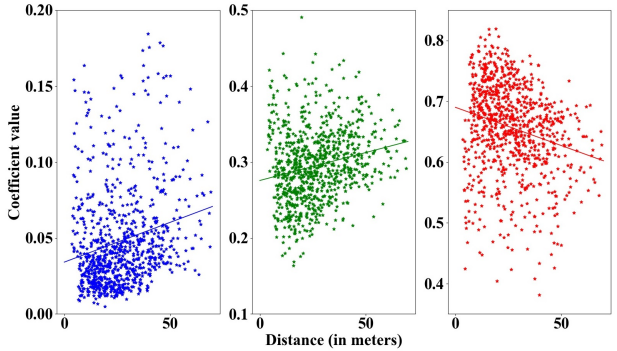


Figure 7. Visualization of the relationship between coefficient vector and object's distance.

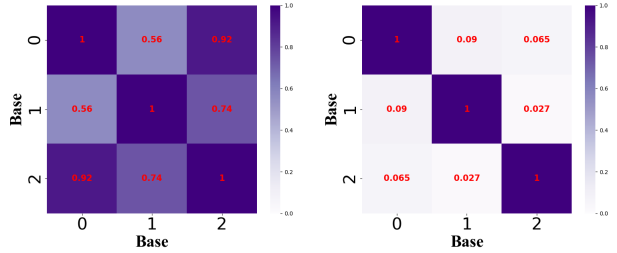


Figure 8. Normalized dot products of our representative tensors. Left: DD-Conv without base similarity loss. Right: DD-Conv with base similarity loss.

References

[1] Garrick Brazil and Xiaoming Liu. M3D-RPN: Monocular 3D region proposal network for object detection. In *Proceedings of the IEEE International Conference on Computer Vision*, pages 9287–9296, 2019. 7, 8

[2] Xiaozihi Chen, Huimin Ma, Ji Wan, Bo Li, and Tian Xia. Multi-view 3D object detection network for autonomous driving. In *IEEE Conference on Computer Vision and Pattern Recognition*, 2017. 2, 6, 7

[3] Zhourong Chen, Yang Li, Samy Bengio, and Si Si. You look twice: GaterNet for dynamic filter selection in CNNs. In *Proceedings of the IEEE Conference on Computer Vision and Pattern Recognition*, pages 9172–9180, 2019. 2

[4] Andreas Geiger, Philip Lenz, and Raquel Urtasun. Are we ready for autonomous driving? the kitti vision benchmark suite. In *2012 IEEE Conference on Computer Vision and Pattern Recognition*, pages 3354–3361. IEEE, 2012. 6

[5] Benjamin Graham, Martin Engelcke, and Laurens van der Maaten. 3D semantic segmentation with submanifold sparse convolutional networks. In *Proceedings of the IEEE Conference on Computer Vision and Pattern Recognition*, pages 9224–9232, 2018. 7

[6] Paul VC Hough. Machine analysis of bubble chamber pictures. In *Conf. Proc.*, volume 590914, pages 554–558, 1959. 2

[7] Max Jaderberg, Karen Simonyan, Andrew Zisserman, et al. Spatial transformer networks. In *Advances in neural information processing systems*, pages 2017–2025, 2015. 2

[8] Xu Jia, Bert De Brabandere, Tinne Tuytelaars, and Luc V Gool. Dynamic filter networks. In *Advances in Neural Information Processing Systems*, pages 667–675, 2016. 2, 3, 5, 7, 8

[9] Jason Ku, Melissa Mozifian, Jungwook Lee, Ali Harakeh, and Steven L Waslander. Joint 3D proposal generation and object detection from view aggregation. In *IEEE/RSJ International Conference on Intelligent Robots and Systems*, pages 1–8, 2018. 2, 6, 7

[10] Alex H Lang, Sourabh Vora, Holger Caesar, Lubing Zhou, Jiong Yang, and Oscar Beijbom. PointPillars: Fast encoders for object detection from point clouds. In *Proceedings of the IEEE Conference on Computer Vision and Pattern Recognition*, pages 12697–12705, 2019. 1, 2, 3, 4, 5, 6, 7

[11] Ming Liang, Bin Yang, Shenlong Wang, and Raquel Urtasun. Deep continuous fusion for multi-sensor 3D object detection. In *Proceedings of the European Conference on Computer Vision (ECCV)*, pages 641–656, 2018. 6, 7

[12] Tsung-Yi Lin, Piotr Dollár, Ross Girshick, Kaiming He, Bharath Hariharan, and Serge Belongie. Feature pyramid networks for object detection. In *Proceedings of the IEEE Conference on Computer Vision and Pattern Recognition*, pages 2117–2125, 2017. 4, 7

[13] Tsung-Yi Lin, Priya Goyal, Ross Girshick, Kaiming He, and Piotr Dollár. Focal loss for dense object detection. In *Proceedings of the IEEE International Conference on Computer Vision*, pages 2980–2988, 2017. 5

[14] Wei Liu, Dragomir Anguelov, Dumitru Erhan, Christian Szegedy, Scott Reed, Cheng-Yang Fu, and Alexander C Berg. SSD: Single shot multibox detector. In *European conference on computer vision*, pages 21–37. Springer, 2016. 7

[15] Charles R Qi, Or Litany, Kaiming He, and Leonidas J Guibas. Deep hough voting for 3D object detection in point clouds. *arXiv preprint arXiv:1904.09664*, 2019. 2

[16] Charles R Qi, Wei Liu, Chenxia Wu, Hao Su, and Leonidas J Guibas. Frustum PointNets for 3D object detection from RGB-D data. In *Proceedings of the IEEE Conference on Computer Vision and Pattern Recognition*, pages 918–927, 2018. 1, 2, 6, 7

[17] Charles R Qi, Hao Su, Kaichun Mo, and Leonidas J Guibas. PointNet: Deep learning on point sets for 3D classification and segmentation. In *IEEE Conference on Computer Vision and Pattern Recognition*, 2017. 1, 2

[18] Charles Ruizhongtai Qi, Li Yi, Hao Su, and Leonidas J Guibas. PointNet++: Deep hierarchical feature learning on point sets in a metric space. In *Advances in Neural Information Processing Systems*, pages 5099–5108, 2017. 1

[19] Shaoshuai Shi, Xiaogang Wang, and Hongsheng Li. PointRCNN: 3D object proposal generation and detection from point cloud. In *Proceedings of the IEEE Conference on Computer Vision and Pattern Recognition*, pages 770–779, 2019. 2

[20] Martin Simonovsky and Nikos Komodakis. Dynamic edge-conditioned filters in convolutional neural networks on graphs. In *Proceedings of the IEEE Conference on Computer Vision and Pattern Recognition*, pages 3693–3702, 2017. 3

[21] Jie Tang, Fei-Peng Tian, Wei Feng, Jian Li, and Ping Tan. Learning guided convolutional network for depth completion. *arXiv preprint arXiv:1908.01238*, 2019. 2, 3

[22] Bei Wang, Jianping An, and Jiayan Cao. Voxel-FPN: Multi-scale voxel feature aggregation in 3D object detection from point clouds. *arXiv preprint arXiv:1907.05286*, 2019. 2, 7

[23] Chen Wang, Danfei Xu, Yuke Zhu, Roberto Martín-Martín, Cewu Lu, Li Fei-Fei, and Silvio Savarese. Densefusion: 6D object pose estimation by iterative dense fusion. In *Proceedings of the IEEE Conference on Computer Vision and Pattern Recognition*, pages 3343–3352, 2019. 1

[24] Jialin Wu, Dai Li, Yu Yang, Chandrajit Bajaj, and Xiangyang Ji. Dynamic filtering with large sampling field for ConvNets. In *Proceedings of the European Conference on Computer Vision (ECCV)*, pages 185–200, 2018. 3

[25] Yan Yan, Yuxing Mao, and Bo Li. SECOND: Sparsely embedded convolutional detection. *Sensors*, 18(10):3337, 2018. 1, 2, 6, 7

[26] Zetong Yang, Yanan Sun, Shu Liu, Xiaoyong Shen, and Jiaya Jia. STD: Sparse-to-Dense 3D object detector for point cloud. *arXiv preprint arXiv:1907.10471*, 2019. 2

[27] Yin Zhou and Oncel Tuzel. VoxelNet: End-to-end learning for point cloud based 3D object detection. In *Proceedings of the IEEE Conference on Computer Vision and Pattern Recognition*, pages 4490–4499, 2018. 1, 2, 6, 7